INTERNATIONAL JOURNAL FOR NUMERICAL METHODS IN FLUIDS, VOL. 20, 887–913 (1995)

A GENERAL ALGORITHM FOR COMPRESSIBLE AND INCOMPRESSIBLE FLOW—PART II. TESTS ON THE EXPLICIT FORM

O. C. ZIENKIEWICZ, K. MORGAN AND B. V. K. SATYA SAI

Institute for Numerical Methods in Engineering, University of Wales, Swansea SA2 8PP U.K.

R. CODINA AND M. VASQUEZ

International Centre for Numerical Methods in Engineering, Techn. University of Catalunya, Barcelona, Spain

SUMMARY

The algorithm introduced in Part I of this paper is applied in its explicit form to a variety of problems in order to demonstrate its wide range of applicability and excellent performance. Examples range from nearly incompressible, viscous, flows through transonic applications to high speed flows with shocks. In most examples linear triangular elements are used in the finite element approximation, but some use of quadratic approximation, again in triangles, indicates satisfactory performance even in the case of severe shocks.

KEY WORDS: compressible flow; CFD (computational fluid dynamics); finite elements in fluids

1. INTRODUCTION

In this part of the paper we shall illustrate on a number of examples the accuracy and generality of the new algorithm presented in Part I,[1] when used in the explicit form. The explicit form is of considerable importance as:

(i) its simplicity makes the computation comparable to other algorithms currently employed and thus allows similar use of adaptivity, remeshing and convergence acceleration procedures (e.g. multigrid techniques);
(ii) in the explicit form, the calculation of $\Delta\rho$ is made directly and no iterative approximation is necessary.

Although full transient solution of incompressible flow problems requires the implicit form of the algorithm, steady-state incompressible flow problems can be solved by simply assuming an artificial compressibility (or the speed of sound) at any convenient value. This does not introduce any additional approximation, but leads to a decoupling of the energy equation.

As mentioned in the previous paper (Part I), the explicit algorithm can be used in its full *two-step* form or it can be simplified (approximated) by a *single-step* operation. The difference in computational cost is small, the single-step scheme being slightly cheaper. Preliminary tests show that both forms are acceptable in practice, in subsonic flow, but for supersonic flow problems, the two-step scheme has been found to give a more stable and accurate result. Thus for all the results presented the two-step scheme has been used.

CCC 0271–2091/95/080887–27

Although the algorithm has a much improved behaviour pattern when compared, for instance, with Taylor–Galerkin and similar alternatives, and can recover mild shocks without additional remedies, for some of the strong shock problems we use either the shock capturing algorithm discussed in Part I or the one described in Reference 2, viz. the pressure switch method.

The general form of the algorithm allows any suitable spatial finite element approximation to be made and in some examples we have used, with success, quadratic shape functions. In a future paper, the use of such higher-order elements will be more fully explored.

2. THE EXPLICIT ALGORITHM—AN ESSENTIAL SUMMARY

We recall the essential form of the algorithm in its semi-discrete form before application of a standard Galerkin space approximation. The details of this space approximation are given in Reference 1 and follow the standard pattern described in many texts.[3]

As we are concerned here, in the explicit form, with the parameter $\theta_2 = 0$, this value if directly used and, for clarity, we have omitted source terms. However, the parameter θ_1 is left in the equations given below, with its value being in the range

$$1/2 \leqslant \theta_1 \leqslant 1$$

as a necessary stability requirement—the value of one-half being used in the examples. Equations (31), (33), (32) and (40) in Reference 1, rewritten now in the semi-discrete, characteristic Galerkin form, define the main solution sequence ($g_i = 0$ is assumed).

Thus from equation (31)

$$\Delta \tilde{U}_i = \Delta t \left[-\frac{\partial (u_j U_i)}{\partial x_j} + \frac{\partial \tau_{ij}}{\partial x_j} + \frac{\Delta t}{2} u_k \frac{\partial^2}{\partial x_k \partial x_j} (u_j U_i) \right]^n \tag{1}$$

From equation (33)

$$\Delta \rho = -\Delta t \left[\frac{\partial U_i}{\partial x_i} + \theta_1 \frac{\partial \Delta \tilde{U}_i}{\partial x_i} - \Delta t \theta_1 \frac{\partial^2 p}{\partial x_i \partial x_i} \right]^n \tag{2}$$

From equation (32)

$$\Delta U_i = \Delta \tilde{U}_i - \Delta t \left[\frac{\partial p}{\partial x_i} - \frac{\Delta t}{2} u_j \frac{\partial^2 p}{\partial x_i \partial x_j} \right]^n \tag{3}$$

And finally from equation (40) (rewritten in time discrete form using the characteristic Galerkin procedure)

$$\begin{aligned} \Delta(\rho E) = & -\Delta t \left[\frac{\partial}{\partial x_i} (u_i \rho E) - \frac{\partial}{\partial x_i} \left(k \frac{\partial T}{\partial x_i} \right) + \frac{\partial}{\partial x_i} (u_i p) - \frac{\partial}{\partial x_i} (\tau_{ij} u_j) \right. \\ & \left. + \frac{\Delta t}{2} u_k \frac{\partial^2}{\partial x_k \partial x_k} (u_i (\rho E + p)) \right]^n \end{aligned} \tag{4}$$

In the above equations, u_i denotes velocities, U_i ($= \rho u_i$) mass fluxes, p pressure, ρ density, E the energy per unit volume and T the absolute temperature.

For an ideal gas, the equation of state

$$p = \rho R T \tag{5}$$

is necessary to close the system and to evaluate the pressure at t_{n+1}. Standard Galerkin

approximation is optimal for the spatial discretization of the equation system (1)–(4) and the details can be found elsewhere.[3]

Starting from known initial conditions at time n, the increments of the problem variables can be found sequentially by a three-step operation. In this

1. the *first step* consists of solving equation (1) for $\Delta\tilde{U}_i$ and
2. the *second step* solves equations (2) and (3) for $\Delta\rho$ and ΔU_i, respectively, using values of $\Delta\tilde{U}_i$ determined in the first step.
3. the third step $\Delta(\rho E)$ is calculated form equation (4) as a transport quantity.

In each of these steps it is necessary to obtain the discretized solution by solving a mass matrix system **M**. This, as is now conventional, is formally avoided by diagonalizing (lumping) this matrix and performing a well-known iterative correction. In Figure 1, we show the form lumping has, for linear and quadratic elements.[3] The *single-step* operation involves the omission of the term $\theta_1 \partial\Delta\tilde{U}_i/\partial x_i$ from equation (2). If this is done, the value of $\Delta\tilde{U}_i$ need not be determined and equations (1) and (3) are combined in a single statement saving a small amount of computer operation and time.

Thus we now approximate equations (1)–(3) by

$$\Delta\rho = -\Delta t\left[\frac{\partial U_i}{\partial x_i} - \Delta t\theta_1 \frac{\partial^2 p}{\partial x_i \partial x_i}\right] \tag{6}$$

$$\Delta U_i = \Delta t\left[-\frac{\partial(u_j U_i)}{\partial x_j} + \frac{\partial \tau_{ij}}{\partial x_j} - \frac{\partial p}{\partial x_i} + \frac{\Delta t}{2} u_k \frac{\partial^2}{\partial x_k \partial x_i}(u_j U_i + p)\right]^n \tag{7}$$

leaving equation (4) unchanged.

3. SPECIALIZATION FOR INCOMPRESSIBILITY

Although the algorithm avoids the interpolation restrictions of the BB condition as shown in Part I, full incompressibility, of course, cannot be dealt with by the explicit form in which a finite speed of sound is assumed if transient computation is required. However, for steady state if we replace $\Delta\rho$ in equation (2) or (6) by

$$\Delta\rho = \frac{1}{c^2}\Delta p \tag{8}$$

and further if we keep ρ as constant in ensuing computation (thus avoiding the equation of state (5)), we note that

(a) the energy equation becomes decoupled, and that
(b) when steady state is reached (and $\Delta p = 0$), the solution is independent of the velocity of sound c, and thus any convenient value can be chosen for this.

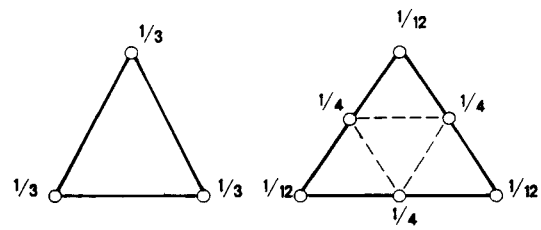

Figure 1. Lumping parameters for linear and quadratic triangles (the last obtained by subdivision into elementary linear triangles)

Thus solving the incompressible flow situation in the manner described above, requires a very few modifications to the basic code. The vector of unknowns now becomes

$$\mathbf{V} = \begin{Bmatrix} u_1 \\ u_2 \\ p \end{Bmatrix} \quad \text{and} \quad \mathbf{F}_i = \begin{Bmatrix} u_1 u_i + \delta_{1i} p \\ u_2 u_i + \delta_{2i} p \end{Bmatrix} \tag{9}$$

and the solution of step II is expressed as

$$\left(\frac{1}{c^2}\mathbf{M} + \Delta t^2 \theta_1 \theta_2 \mathbf{H}\right)\left(\frac{\Delta \bar{p}}{\Delta t}\right) = -\left[\mathbf{Q}\{u_i\}^n + \theta_1(\Delta \tilde{u}_i)\right] + \Delta t \theta_1 \mathbf{H} \bar{p}^n] \tag{10}$$

where

$$\mathbf{M} = \int_\Omega \mathbf{N}^{\mathrm{T}} \mathbf{N} \, \mathrm{d}\Omega \tag{11}$$

$$\mathbf{H} = \int_\Omega \frac{\partial \mathbf{N}^{\mathrm{T}}}{\partial x_i} \frac{\partial \mathbf{N}}{\partial x_i} \mathrm{d}\Omega \tag{12}$$

$$\mathbf{Q} = \int_\Omega \mathbf{N}^{\mathrm{T}} \frac{\partial \mathbf{N}}{\partial x_i} \mathrm{d}\Omega \tag{13}$$

However, for fully incompressible flow problems $c \to \infty$ and equation (13) can be solved only if $\Delta t^2 \theta_1 \theta_2 \mathbf{H}(\Delta \bar{p}/\Delta t)$ is not ignored; i.e. for fully incompressible flow problems only a semi-implicit form can be used. However, if one is interested only in the steady-state results, one could use an artificial compressibility (a finite speed of sound) and still use the fully explicit form of equation (10), omitting the Laplacian term on the left-hand side. Even though the steady-state result does not depend on the value of c assumed, it is reasonable to assume a high value of c (Mach number $\simeq 0{\cdot}2$ is convenient).

4. THE TIME INCREMENTS

For every element the critical time step $\Delta t^{(1)}_{\text{crit}}$ corresponding to the convective terms is calculated using equation (19) of Part I. Similarly, $\Delta t^{(2)}_{\text{crit}}$, corresponding to sonic speed is evaluated.

Without viscosity, the orders of magnitude of these steps are

$$\begin{aligned} \Delta t^{(1)}_{\text{crit}} &\equiv \frac{h}{|u|} \\ \Delta t^{(2)}_{\text{crit}} &\equiv \frac{h}{(|u| + c)} \end{aligned} \tag{14}$$

For fully transient computations the minimum value of these time steps will determine the maximum Δt that can be used with stability. However, if the determination of steady-state solution only is desired, so-called *local time stepping* could be adopted. This device conventionally used simply determines, at each node, the minimum value of $\Delta t^{(1)}_{\text{crit}}$ or $\Delta t^{(2)}_{\text{crit}}$ and uses it at that node together with a lumped mass matrix (which of course does not change the accuracy of the final solution). The use of local time stepping is, of course, totally equivalent to using a constant time step throughout the whole domain and adjusting the mass matrix coefficient suitably.

Again if steady state only is sought, it is convenient to determine the 'interior Δt^*' (that occurring inside the square brackets of equations (1)–(4)) on a basis leading to optimal steady-

state results. This has been determined elsewhere[3] by comparison of the Petrov–Galerkin and characteristic Galerkin procedures as requiring that

$$\Delta t^* = \frac{h}{|u|} \tag{15}$$

(in the absence of viscosity) or generally

$$\Delta t^* = \Delta t^{(1)}_{\text{crit}} \tag{16}$$

5. NUMERICAL EXAMPLES

In order to study the performance of the algorithm, the present scheme has been applied to a variety of problems in its fully explicit form. First, however, a comparison of the performance of the two versions of the scheme, namely, the version with the intermediate step and the version without the intermediate step, has been carried out. Later, a variety of problems, both in subsonic and supersonic regimes, have been dealt with. A slightly modified version of the code has been used for validating the scheme for incompressible flow problems.

5.1. Comparison exercise

These examples are to study the performance of the two schemes discussed in Part I, viz. the scheme with the intermediate step (also referred to in this paper as scheme I) and the scheme without the intermediate step (also referred to in this paper as scheme II). For this purpose, subsonic inviscid flow at a Mach number 0·5 and angle of attack 0° past a NACA0012 aerofoil is first considered. Figure 2(a) shows the mesh used which consists of 969 nodes and 1824 elements and Figure 2(b) shows the mesh refinement near the aerofoil surface. The time evolution of non-dimensional density at the leading edge of the aerofoil is plotted in Figure 2(c) for both the schemes. It is observed that there is little or no difference in the behaviour of the two schemes. In either of the schemes $\Delta t_{(\text{interior})} \neq \Delta t_{(\text{exterior})}$, and they are given as below:

$$\Delta t_{(\text{exterior})} = \beta \Delta t^{(2)}_{\text{crit}}$$

(where β is a safety factor $\sim 0{\cdot}9$)

$$\Delta t_{(\text{interior})} = \Delta t^{(1)}_{\text{crit}}$$

It is also observed that both the schemes converge to the same result and also the time taken (CPU requirement) is almost the same, with scheme II being slightly cheaper.

A further study of the scheme with the intermediate step has been made by considering the cases of $\Delta t_{(\text{interior})} = \Delta t_{(\text{exterior})}$ and $\Delta t_{(\text{interior})} \neq \Delta t_{(\text{exterior})}$. As expected when $\Delta t_{(\text{interior})} = \Delta t_{(\text{exterior})} = \beta \Delta t^{(1)}_{\text{crit}}$ the time taken to reach the steady state is longer than that for the case of $\Delta t_{(\text{interior})} \neq \Delta t_{(\text{exterior})}$. This is shown in Figure 2(d). However a significant difference in the steady-state values is observed for the two cases as indeed may be expected with the use of non-optimal upwind parameters implied by the external time step and indeed the second option is most accurate.

To further check the performance of the two schemes, supersonic flow past NACA0012 with Mach number 1·2 and angle of attack 0° has been considered. The mesh used for this problem is shown later in Figure 6. Unlike in the previous example, here a larger difference in the performance can be observed. The time evolution of density at the leading edge has been plotted, once again, for both schemes and is shown in Figures 3(a) and 3(b). Scheme II shows oscillations

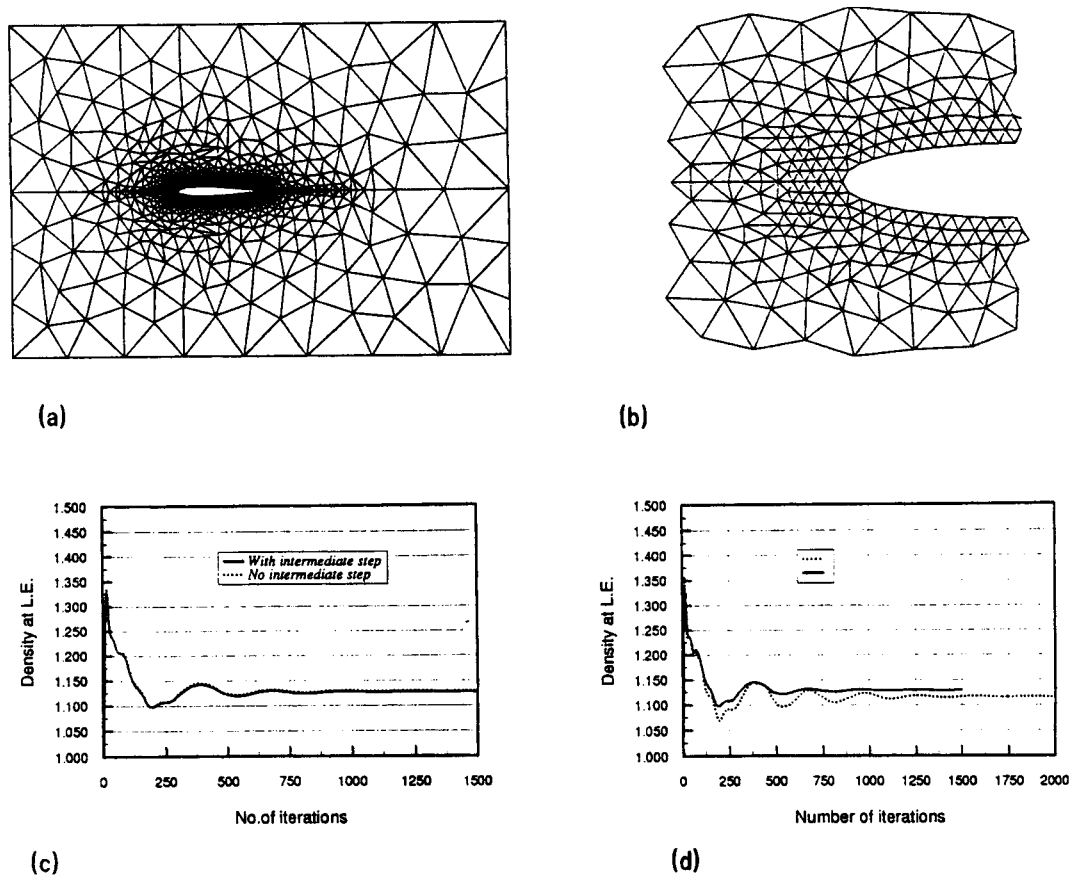

Figure 2. Subsonic inviscid flow past NACA0012 aerofoil with $M_\infty = 0{\cdot}5$ and $\alpha = 0°$: (a) mesh for the comparison exercise (no. of nodes = 969, no of elements = 1824); (b) mesh refinement near the surface of the aerofoil; (c) time evolution of density at leading edge for the two schemes; (d) effect of Δt terms on the performance of scheme I. (. . . .) $\Delta t_{\text{interior}} = \Delta t_{\text{exterior}} = \Delta t^{(2)}_{\text{crit}}$; (—) $\Delta t_{\text{interior}} = \Delta t^{(1)}_{\text{crit}}$ and $\Delta t_{\text{exterior}} = \beta \Delta t^{(2)}_{\text{crit}}$

even though the final (mean) result is nearly the same as that given by scheme I. In view of these findings, for all the subsequent problems only scheme I (with different Δt's for steady state) has been used.

To compare the present results (for $M = 0{\cdot}5$) with those obtained by the Taylor–Galerkin (T–G) scheme, a code based on the latter has also been run on the same mesh. Figure 4(a) and 4(b) show the pressure contours with the T–G scheme with an artificial viscosity(C_s) of 0 and 0·5, respectively, and Figure 4(c) shows the results with the present scheme (with no artificial viscosity). In all these figures, the right side ones show the pressure contours on an enlarged scale near the leading edge. It may be observed that the oscillations near the leading edge of the aerofoil for $C_s = 0{\cdot}0$ are not present when the present scheme is employed. Similarly, Figures 5(a) and 5(b) show the density contours obtained by the T–G scheme near the leading edge with $C_s = 0{\cdot}0$ and $C_s = 0{\cdot}5$, respectively, and Figure 5(c) shows the same with the present scheme. Once again a comparison of these three figures reveals the superiority of the present scheme. Figure 5(d) shows a plot of density along the stagnation line of the above three results. Table I shows the

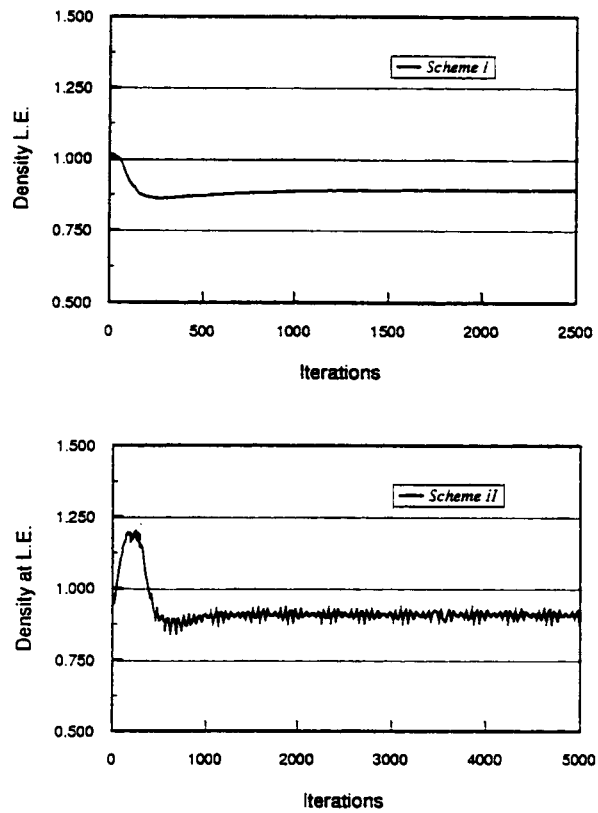

Figure 3. Supersonic inviscid flow past NACA0012 aerofoil with $M_\infty = 1{\cdot}2$ and $\alpha = 0°$: (a) time evolution of density at leading edge with scheme I; (b) time evolution of density at leading edge with scheme II

comparison of different non-dimensional flow variables at the leading edge of the aerofoil obtained with the present scheme ($C_s = 0{\cdot}0$), T–G scheme ($C_s = 0{\cdot}5$) and the analytical result. From the table it could be inferred that, in general, the predictions by the present scheme are more accurate than those of the Taylor–Galerkin scheme.

5.2. Transonic inviscid flow past NACA0012 at 0° angle of attack

The next problem considered is transonic flow past NACA0012 aerofoil at Mach number 0·95 and angle of attack 0°. Figure 6(a) shows the domain and grid considered and Figure 6(b) shows the mesh refinement near the surface of the aerofoil. The mesh consists of 3753 nodes and 7351 elements. The inflow and outflow boundaries are situated at a distance of 12 chords from the surface of the aerofoil. Figure 7(a) shows the pressure contours. These follow the same trend as reported by AGARD working group 07.[4] It may be pointed out that the results of Reference 4 were obtained by considering 561 points on the surface of the aerofoil, while in the present study only 66 points were employed on the surface of the aerofoil. The fish tail shock, in which the two oblique shocks off the trailing edge meet the weak normal shock downstream, is reasonably well predicted. Figure 7(b) shows a comparison of the distribution of coefficient of pressure on the

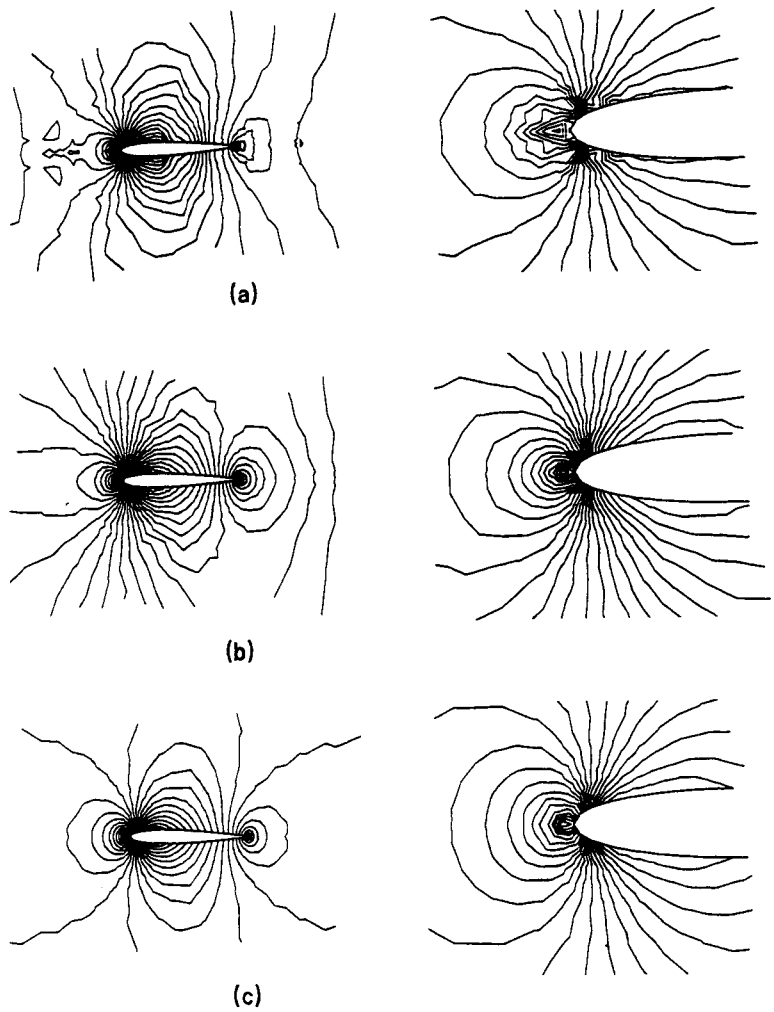

Figure 4. Subsonic inviscid flow past NACA0012 aerofoil with $M_\infty = 0{\cdot}5$ and $\alpha = 0°$ (pressure contours): (a) Taylor–Galerkin scheme with $C_s = 0{\cdot}0$; (b) Taylor–Galerkin scheme with$C_s = 0{\cdot}5$; (c) present scheme with $C_s = 0{\cdot}0$

Table I. Comparison of numerical schemes with analytical results (flow variables at stagnation point)

Variable	Analytical	Present	T–G scheme
Density	1·1297	1·1268	0·98913
Pressure	3·3891	3·2195	2·9726
Temperature	10·5	10·347	10·5186

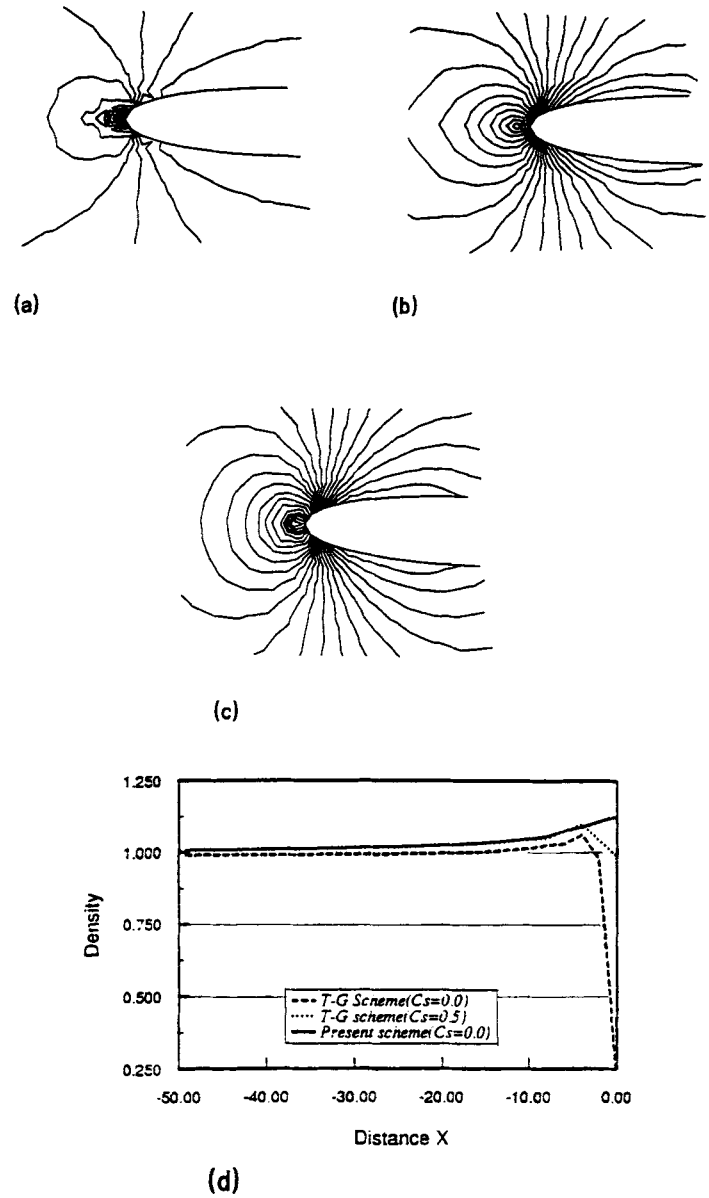

Figure 5. Subsonic inviscid flow past NACA0012 aerofoil with $M_\infty = 0{\cdot}5$ and $\alpha = 0°$: (a) density contours with the T–G scheme with $C_s = 0{\cdot}0$; (b) density contours with the T–G scheme with $C_s = 0{\cdot}5$; (c) density contours with present scheme with $C_s = 0{\cdot}0$; (d) variation of density along stagnation line

surface of the aerofoil with the results given in Reference 4. It can be observed that there is a good agreement between the two results over most of the surface. Also plotted is the result obtained with the T–G scheme with the same mesh and with $C_s = 0{\cdot}5$. In the present scheme a $C_s = 0{\cdot}25$ has been used to avoid small oscillations in the shock region. The present result is in excellent agreement with the T–G scheme.

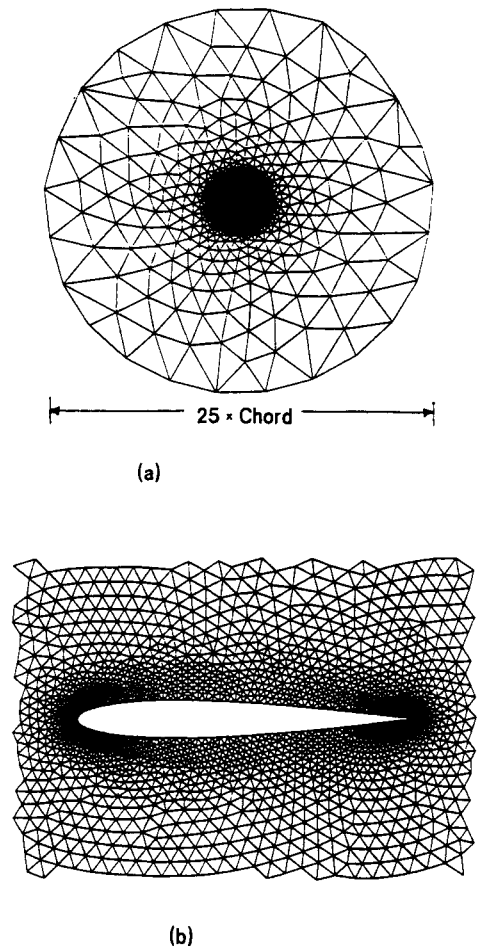

Figure 6. Transonic and supersonic flows past NACA0012 aerofoil: (a) overall mesh: no of nodes = 3753, no of elements = 7351; (b) mesh refinement near the surface of the aerofoil

5.3. Subsonic flow past NACA0012 at 1·2° angle of attack

The mesh employed for this problem is the same as that for the transonic flow case. A Mach number of 0·85 and an angle of attack of 1·2° are prescribed. An artificial viscosity with $C_s = 0{\cdot}25$ has been used. A far-field vortex correction is employed to account for the effect of circulation on the far-field boundary conditions very much in the same way as done in Reference 4. Figure 8(a) shows the pressure contours and Figure 8(b) shows Mach number contours. Figure 8(c) shows a plot of the entropy deviation contours. A maximum entropy deviation of 0·5883 has been observed at the iocation of the shock on the suction side of the aerofoil. This is shown in Figure 8(d). Figure 9(a) shows the adaptive mesh obtained from the original result. The methodology for adaptivity is based on the first derivative error measure and details can be obtained from Reference 5. An improvement in the shock details can be seen in Figure 9(b) as a result of the adaptivity. Figure 10(a) shows a comparison of coefficient of pressure along the two sides of the

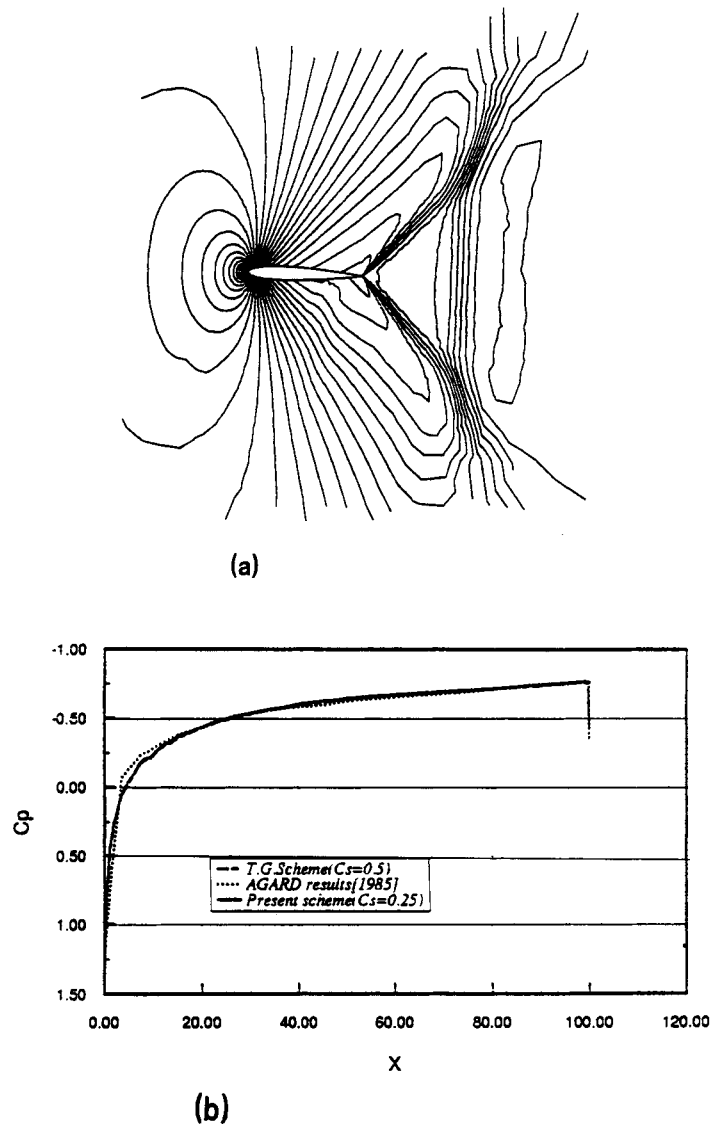

Figure 7. Transonic inviscid flow past NACA0012 with $M_\infty = 0{\cdot}95$ and $\alpha = 0°$: (a) pressure contours with the present scheme; (b) comparison of pressure coefficient on aerofoil surface with other results

aerofoil with the present scheme with the original mesh and that of Reference 4. Also shown in Figure 10(a) is the result obtained by Hassan *et al.*,[6] with the same mesh. While on the suction side the present result and that of Reference 6 seem to agree with each other and differ from that of Reference 4, on the pressure side all the three results seem to differ from one another. Especially, discrepancy is observed at the locations of the shock fronts. Part of the discrepancy could be attributed to the errors in reproducing the result of Reference 4 from their plots. A further improvement in the results is obtained with adaptivity and is shown in Figure 10(b). The following are the values of coefficient of lift (C_L) and coefficient of drag (C_D) obtained by the

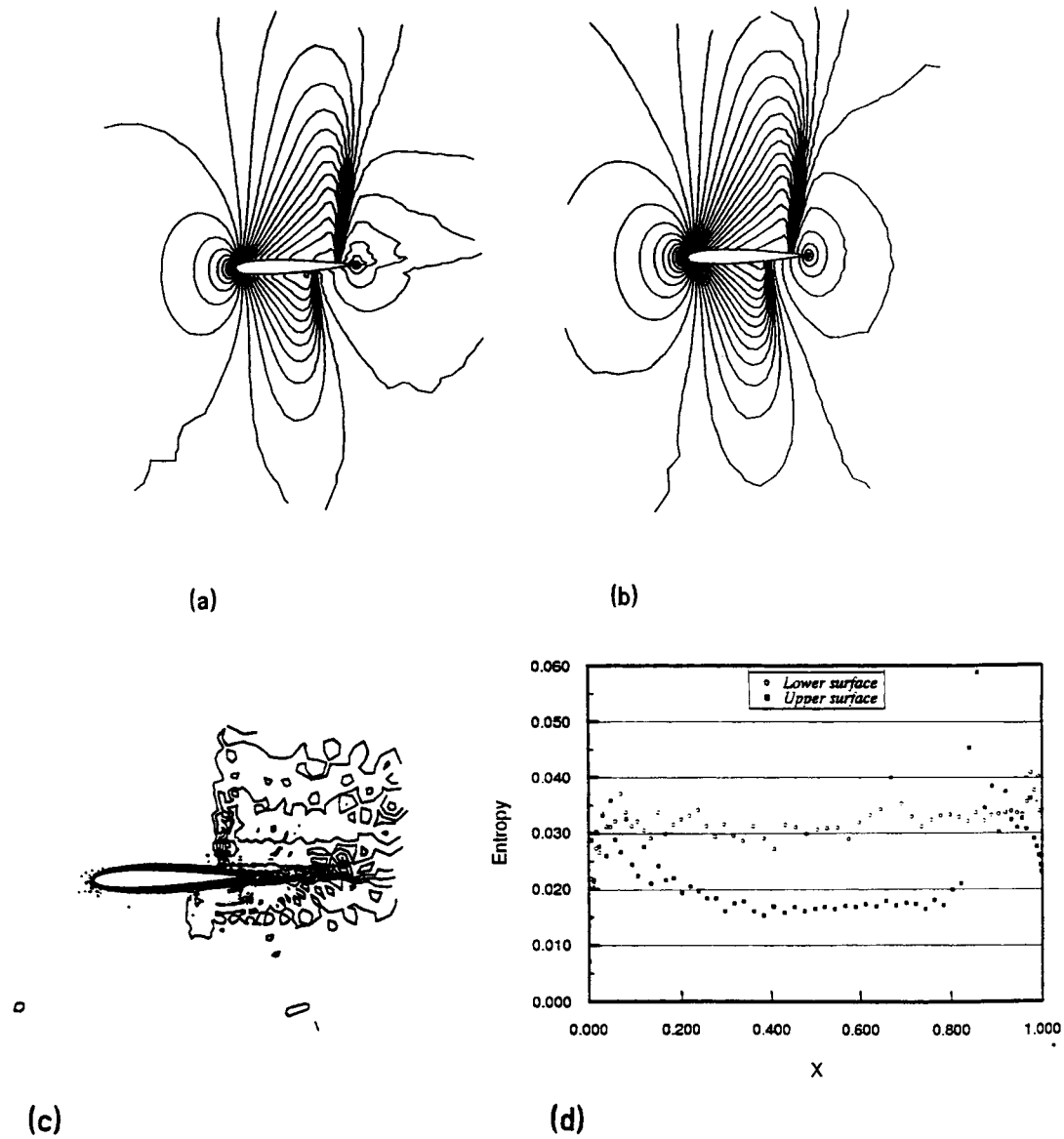

Figure 8. Inviscid flow past NACA0012 with $M_\infty = 0{\cdot}85$ and $\alpha = 1{\cdot}2°$: (a) pressure contours; (b) Mach number contours; (c) entropy deviation contours; (d) entropy deviation plot on the surface of the aerofoil

present method:

$$C_L = 0{\cdot}3437, \quad C_D = 0{\cdot}5234$$

5.4. Supersonic inviscid flow past NACA0012 at 0° angle of attack

The last aerofoil problem considered is the case of supersonic inviscid flow past NACA0012 aerofoil with Mach number 1·2 and 0° angle of attack. The same mesh as in the previous two cases

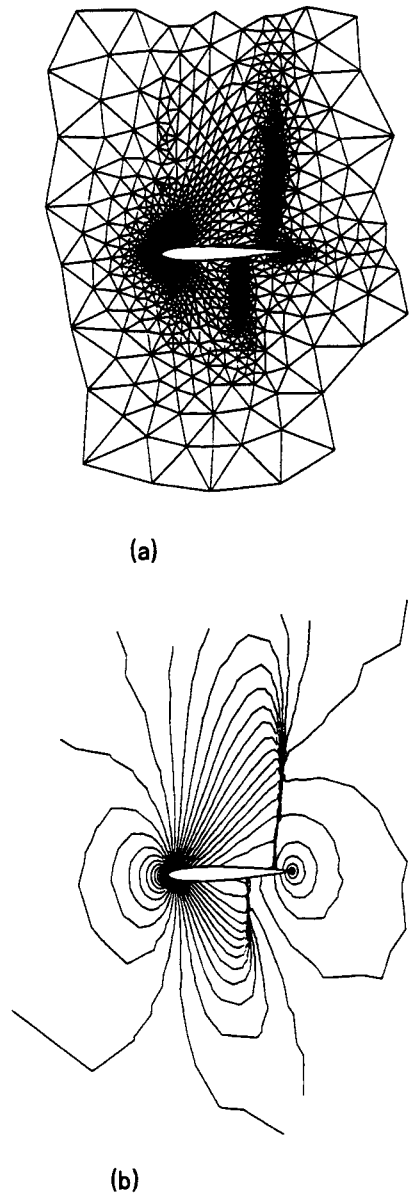

Figure 9. Adaptive results for inviscid flow past NACA0012 with $M_\infty = 0{\cdot}85$ and $\alpha = 1{\cdot}2°$: (a) mesh: no of nodes = 2822, no. of elements = 5512; (b) pressure contours

has been again used for this case. Some artificial viscosity ($C_s = 0{\cdot}25$) has been used. Figures 11(a) and 11(b) show the pressure contours and Mach contours. A bow shock in the front and two oblique shocks off the trailing edge are captured well. Figure 11(c) shows a plot of the coefficient of pressure along the surface of the aerofoil. Good agreement can again be observed with Reference 4. The adaptive mesh for this problem is shown in Figure 11(d) and the pressure contours and Mach number contours with adaptivity are shown in Figures 11(e) and 11(f)

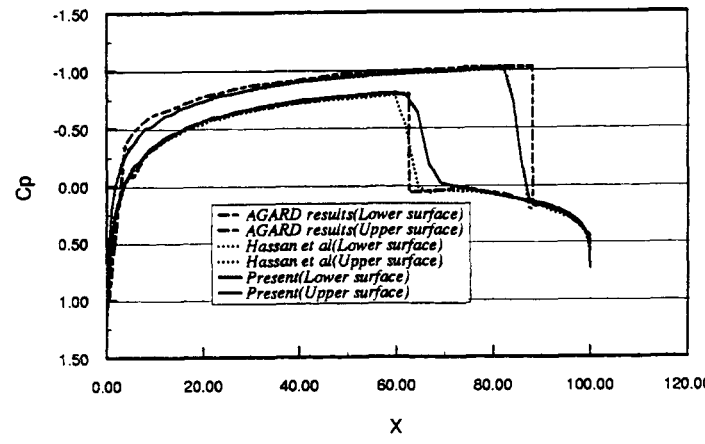

Figure 10. Inviscid low past NACA0012 with $M_\infty = 0{\cdot}85$ and $\alpha = 1{\cdot}2°$: (a) C_p distribution with the original mesh; (b) C_p distribution with the adaptive mesh

respectively. A much sharper shock is, of course, observed in these two figures. It is of interest to observe that the effect of adaptive refinement on the aerofoil pressure distribution is here negligible.

5.5. Supersonic inviscid flow past a circular cylinder

Figure 12(a) shows the mesh used for the problem of inviscid flow past a circular cylinder at a Mach number 2·0. Only 1/4 of the geometry has been considered. The mesh consists of 987 nodes and 1845 elements. An artificial viscosity of 0·25 has been used for this case. Also the Taylor–Galerkin scheme with $C_s = 0{\cdot}50$ has been applied for the same geometry. Figure 12(b) shows the pressure contours for this case. The adaptive mesh is shown in Figure 12(c) and the

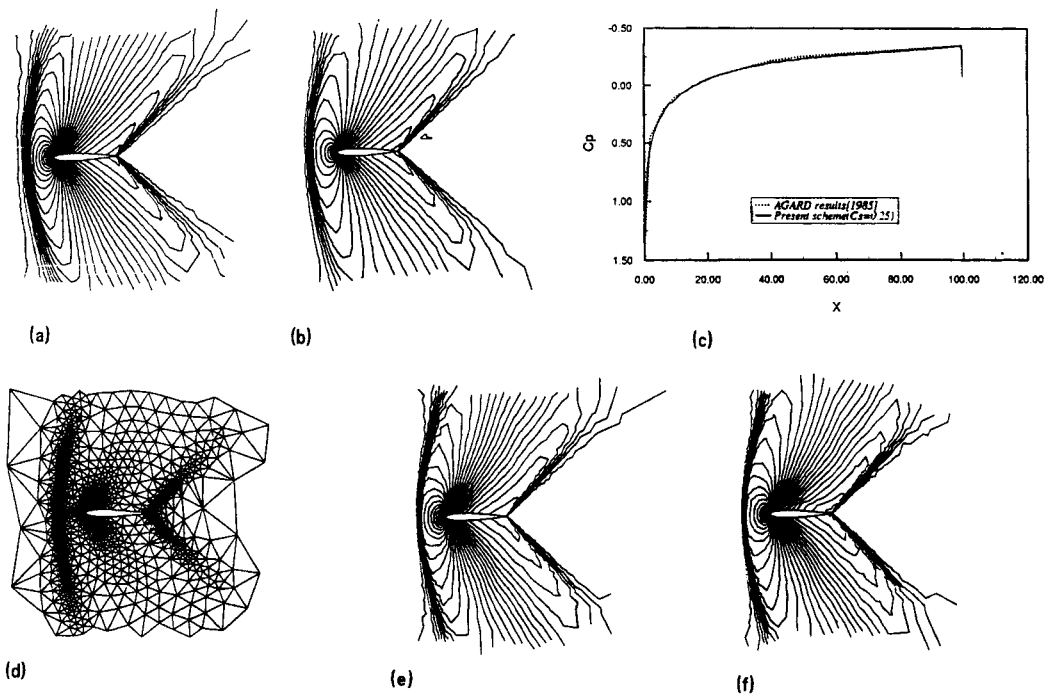

Figure 11. Supersonic inviscid flow past NACA0012 aerofoil with $M_\infty = 1{\cdot}2$ and $\alpha = 0°$: (a) pressure contours; (b) Mach number contours; (c) comparison of coefficient of pressure with other results; (d) adaptive mesh: no. of nodes = 1920, no. of elements = 3728; (e) pressure contours with the adaptive mesh; (f) Mach number contours with the adaptive mesh

resulting pressure contours are shown in Figure 12(d). The adaptivity, once again, is seen to result in a sharper shock in front of the cylinder. Figures 12(e) and 12(f) show the Mach number contours with the original mesh and the adaptive mesh, respectively. A comparison of the coefficient of pressure obtained by different methods is shown in Figure 12(g). It may be observed that the shock layer as predicted by the present scheme (with the original mesh) is slightly sharper than that obtained by the Taylor–Galerkin scheme.

5.6. One-dimensional steady shock problem—linear and quadratic elements

This example is to illustrate the application of higher-order elements for the present scheme. The one-dimensional geometry is modelled as a special case of a two-dimensional problem with an array of linear or quadratic rectangular elements in the X-direction. The following set of values have been prescribed at the inlet and outlet:

Inflow (supersonic)	*Outflow (subsonic)*
Density: 1·0	Density: 2·66667
Temperature: $6{\cdot}2306 \times 10^{-4}$	
X-velocity: 1·00	
Y-velocity: 0·0	
Mach number: 2·0	

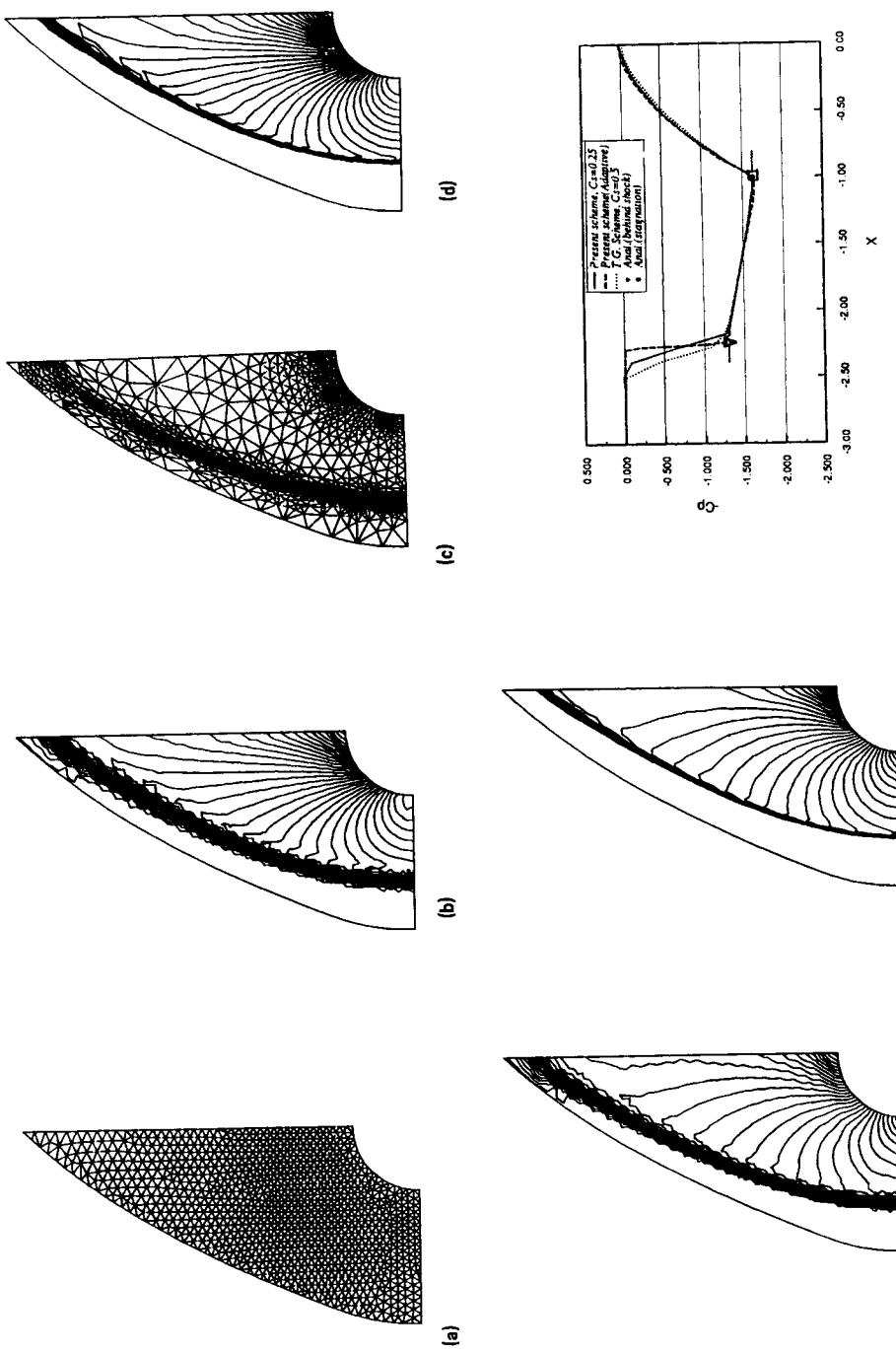

Figure 12. Supersonic inviscid flow past a circular cylinder with $M_\infty = 2{\cdot}0$: (a) mesh: no. of nodes = 987, no. of elements = 1845; (b) pressure contours; (c) adaptive mesh: no. of nodes = 950, no. of elements = 1793; (d) pressure contours with the adaptive mesh; (e) Mach number contours with the original mesh; (f) Mach number contours with the adaptive mesh; (g) comparison of coefficient of pressure with other results

Both linear rectangles (with 80 nodes and 39 elements) and quadratic rectangles (with 81 nodes and 13 elements) have been used for the discretization although the problem is one-dimensional. The shock capturing technique described in Reference 1 has been used in this case. After the steady shock is obtained, various parameters have been plotted along the length of the geometry to illustrate the results. Figures 13(a) to 13(d) show the pressure variation along the axis with and without using the shock capturing technique described in Part I. The upper figures show the performance with linear rectangular elements and the bottom figures show the performance with quadratic rectangles. Similarly, Figures 14, 15 and 16 show the variation of density, Mach number and temperature, respectively, along the same line. In all these figures it may be observed that the quadratic elements yield better results than the linear elements. Also an improvement in the results with the use of the shock capturing technique can be seen.

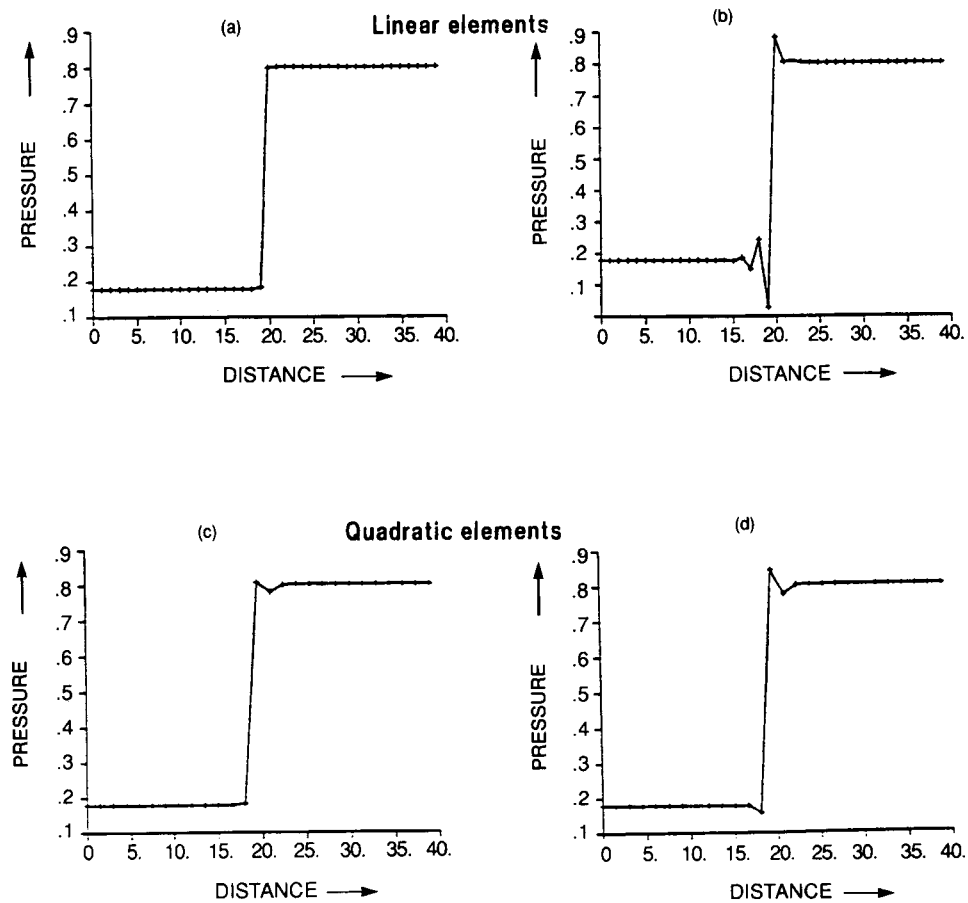

Figure 13. 1-D steady shock problem (pressure along length of the geometry): (a) linear rectangles and with shock capturing; (b) linear rectangles and without shock capturing; (c) quadratic rectangles and with shock capturing; (d) quadratic rectangles and without shock capturing

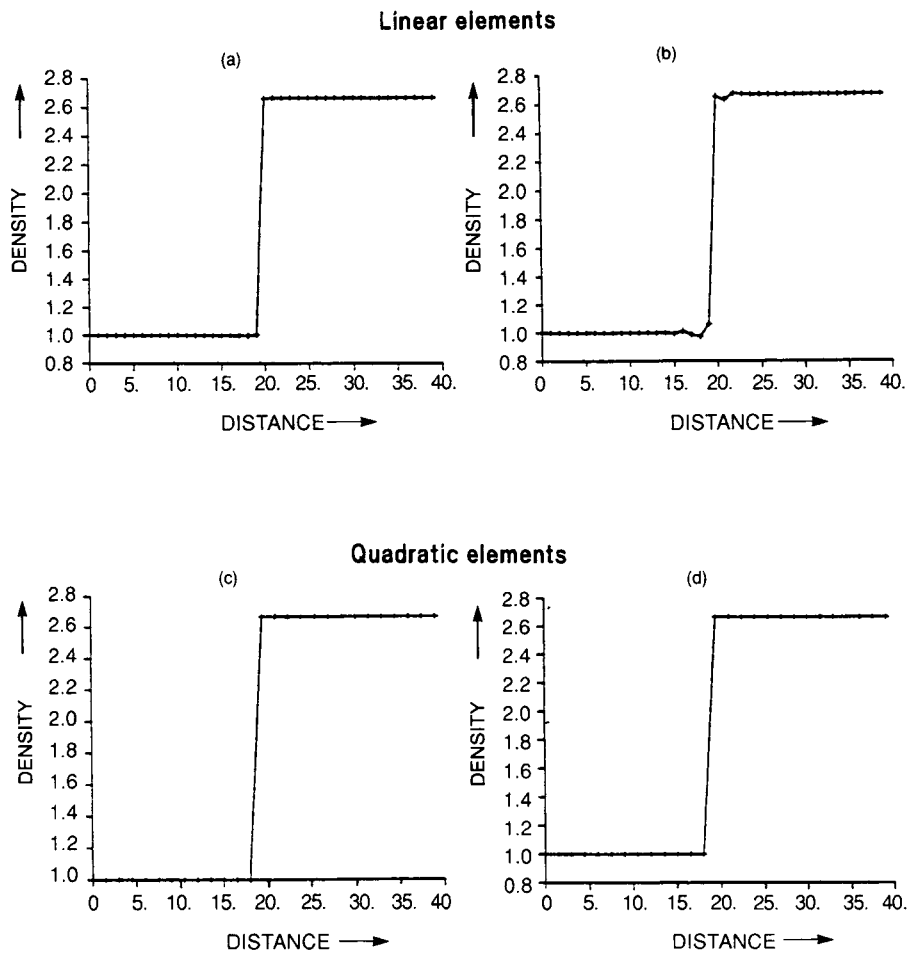

Figure 14. 1-D steady shock problem (density along length of the geometry): (a) linear rectangles and with shock capturing; (b) linear rectangles and without shock capturing; (c) quadratic rectangles and with shock capturing; (d) quadratic rectangles and without shock capturing

5.7. Supersonic inviscid flow past a wedge—linear and quadratic elements

This example is again designed to test linear and quadratic elements and deals with the supersonic inviscid flow past a 15° wedge at a Mach number 3·0. Figures 17(a) and 17(b) show the discretization of the domain into linear triangles (with 1621 nodes and 3099 elements) and quadratic triangles (with 758 nodes and 1587 elements), respectively. The following values have been prescribed at the inlet:

Density: 1·0
Temperature: 10·0
X-velocity: 3·55
Y-velocity: 0·0
Mach number: 3·0

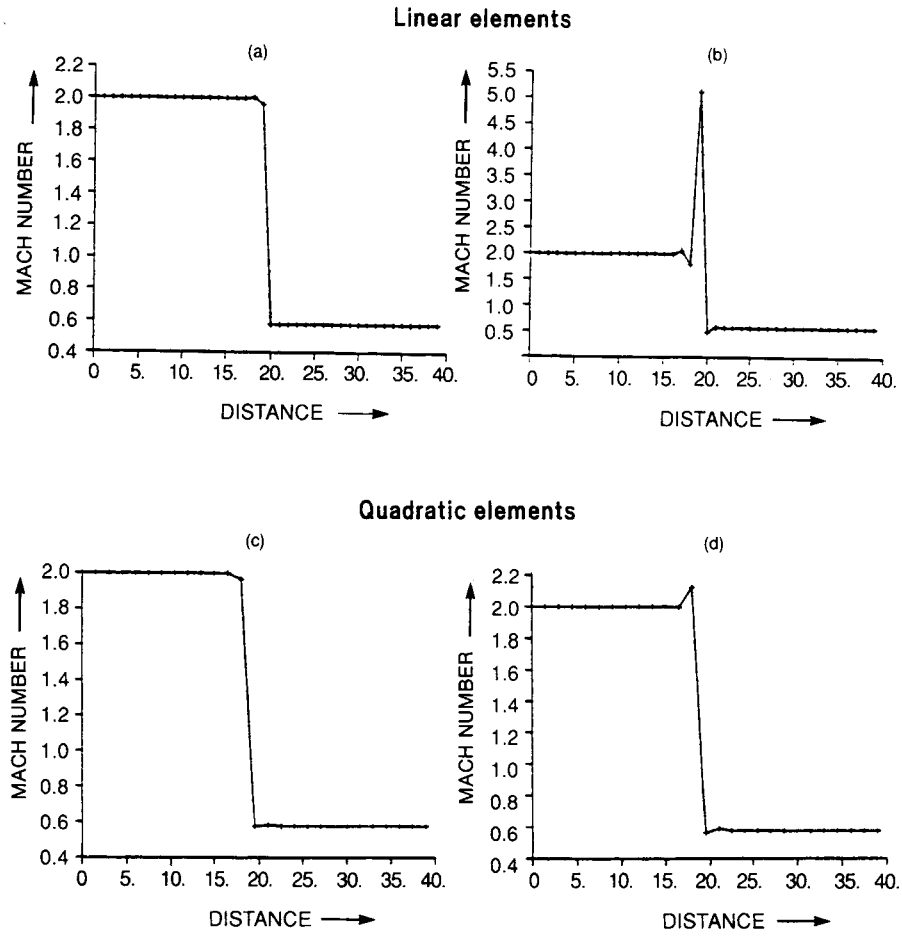

Figure 15. 1-D steady shock problem (Mach number along length of the geometry): (a) linear rectangles and with shock capturing; (b) linear rectangles and without shock capturing; (c) quadratic rectangles and with shock capturing; (d) quadratic rectangles and without shock capturing

Once again, the shock capturing technique of Part I has been employed in this example. Steady-state contours for pressure, density, Mach number and temperature are presented in the ensuing figures. Also, a section A–A, cutting across the geometry as shown in Figure 17, is considered and various parameters along the same are presented. While Figures 18(a) and 18(b) show the pressure contours with linear and quadratic triangular elements, respectively, Figures 18(c) and 18(d) show the variation of pressure along the section A–A for the two types of elements, respectively. Similar plots for density, Mach number and temperature are given in Figures 19, 20 and 21, respectively. These figures suggest that, even in the presence of shocks, quadratic elements give good performance.

5.8. Inviscid incompressible flow past NACA0012 aerofoil at 0° angle of attack

All the examples considered so far have demonstrated the ability of the present scheme to deal with compressible flow situations ranging from subsonic flows to supersonic flows. In this and the

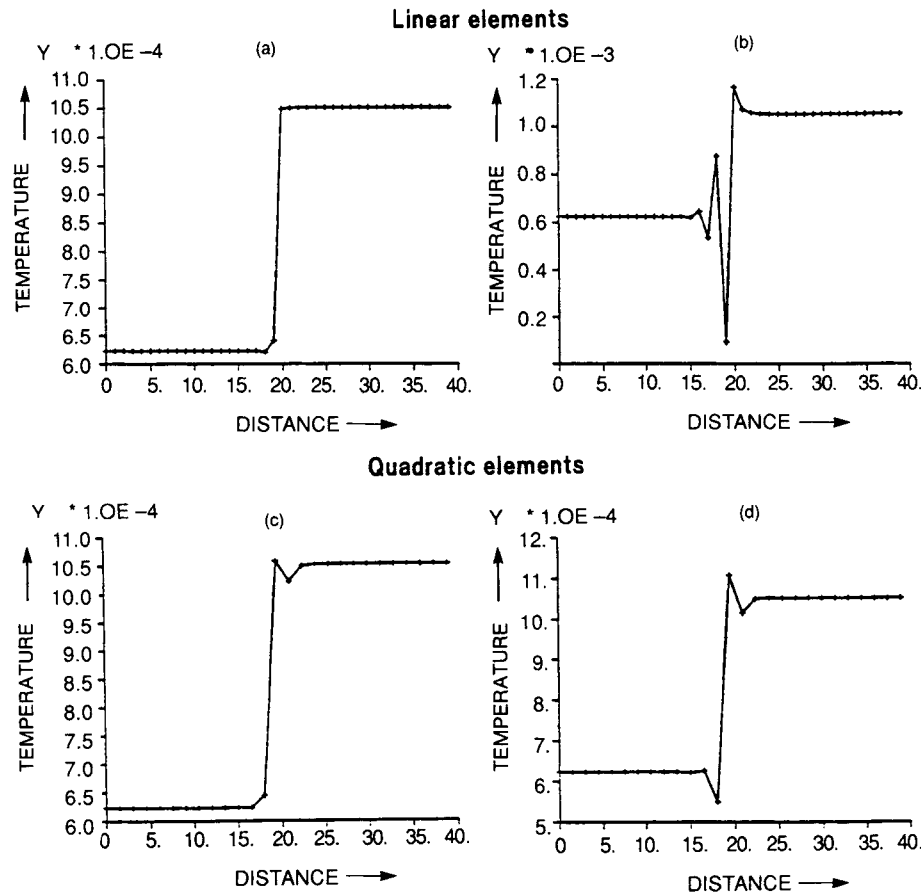

Figure 16. 1-D steady shock problem (temperature along length of the geometry): (a) linear rectangles and with shock capturing; (b) linear rectangles and without shock capturing; (c) quadratic rectangles and with shock capturing; (d) quadratic rectangles and without shock capturing

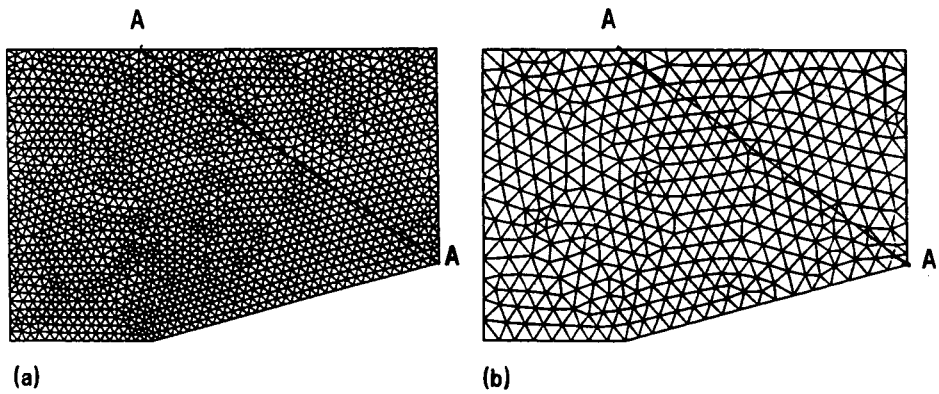

Figure 17. Geometry for the supersonic inviscid flow past a 15° wedge with $M_\infty = 3{\cdot}0$: (a) mesh with linear triangular elements: no. of nodes = 1621, no. of elements = 3099; (b) mesh with quadratic triangular elements: no. of nodes = 1587, no. of elements = 758

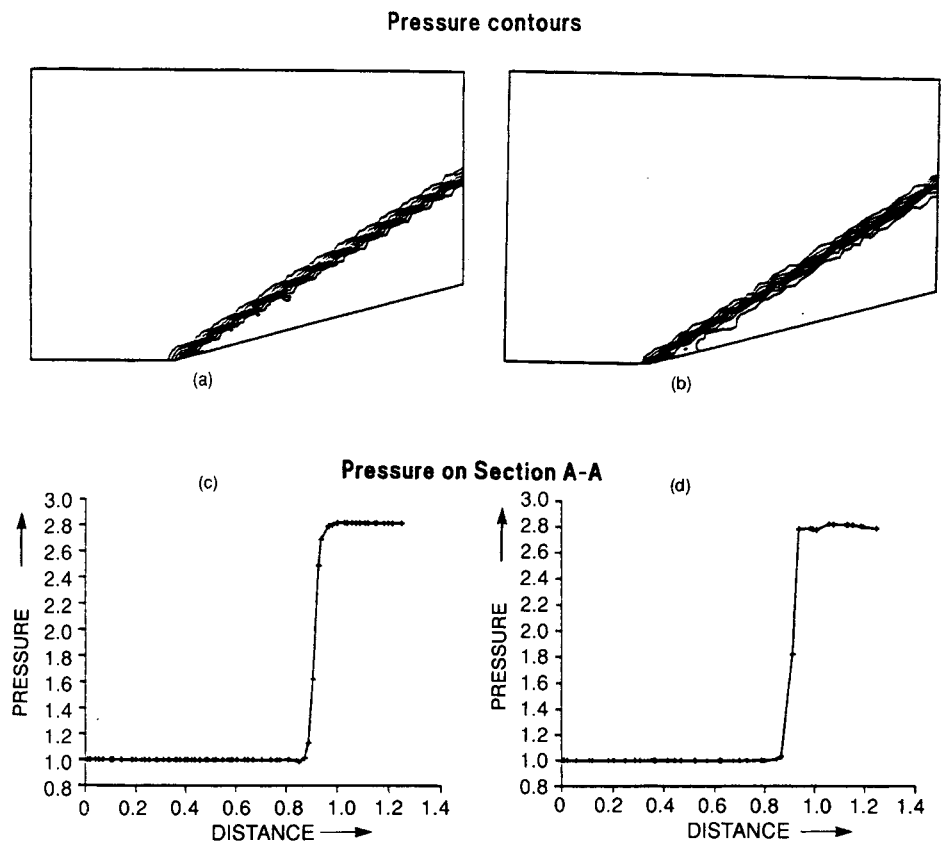

Figure 18. Problem of Figure 17 continued (pressure): (a) contours with linear triangular elements; (b) contours with quadratic triangular elements; (c) distribution along the section with linear triangular elements; (d) distribution along the section with quadratic triangular elements

next examples we present the results obtained by applying the present scheme to incompressible flow situations in steady state. The strategy for dealing with these problems has been discussed in Section 3. The first of these examples is inviscid, incompressible flow past NACA0012 aerofoil at 0° angle of attack. The mesh used for this problem is the same as that used for the subsonic flow problem ($M = 0{\cdot}5$) in Figure 2. Figure 22(a) shows the streamline contours at steady state and Figure 22(b) shows the pressure contours. The streamlines follow the same trend as predicted by the potential flow theory. A comparison of the coefficient of pressure distribution on the surface of the aerofoil with that obtained by potential flow theory is presented in Figure 22(c).

5.9. Viscous, incompressible flow in a lid driven cavity

This last example—the case of lid driven cavity—is considered as a standard test for viscous, incompressible flow. No slip condition is assumed on all the walls. A pressure datum $p = 0$ is specified at the mid-point of the bottom wall. The case of $Re = 100$ is considered. Figure 23(a) shows a nearly uniform mesh of 1310 nodes and 2482 elements used for this problem. Figures 23(b), 23(c) and 23(d) show the pressure contours, velocity contours and the stream function

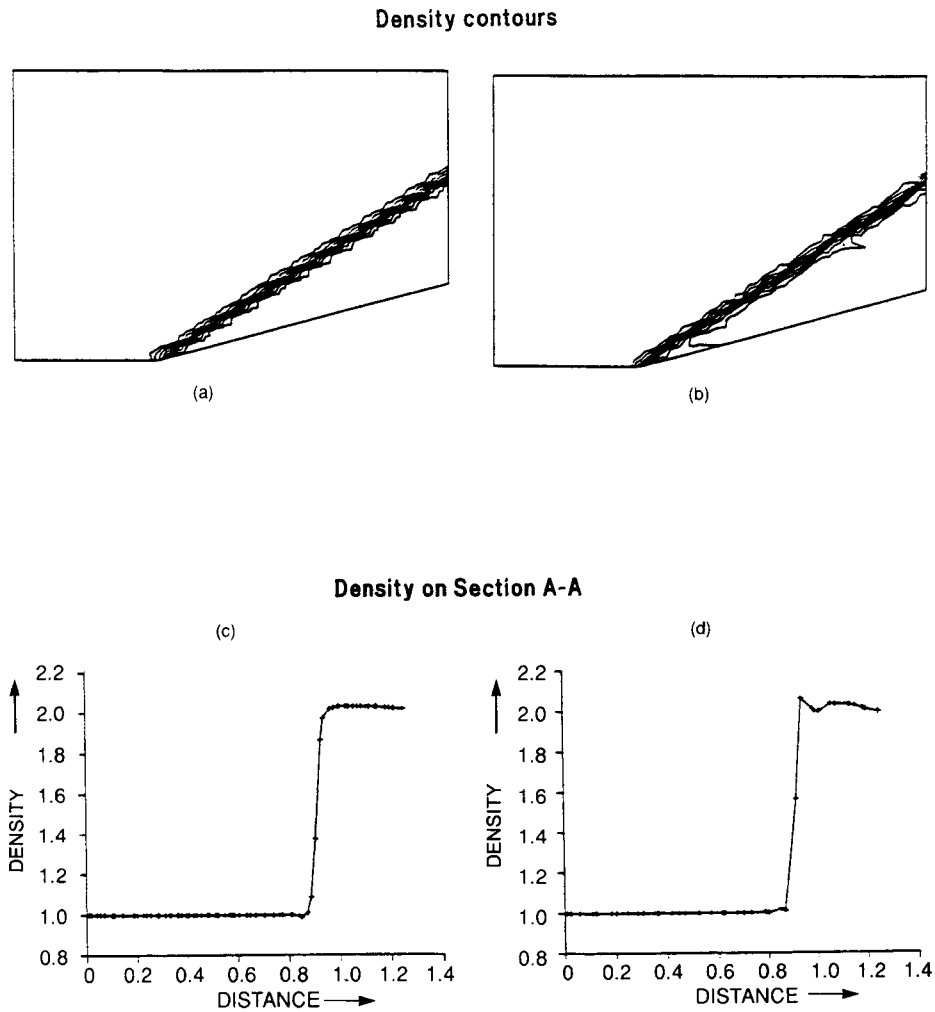

Figure 19. Problem of Figure 17 continued (density): (a) contours with linear triangular elements; (b) contours with quadratic triangular elements; (c) distribution along the section with linear triangular elements; (d) distribution along the section with quadratic triangular elements

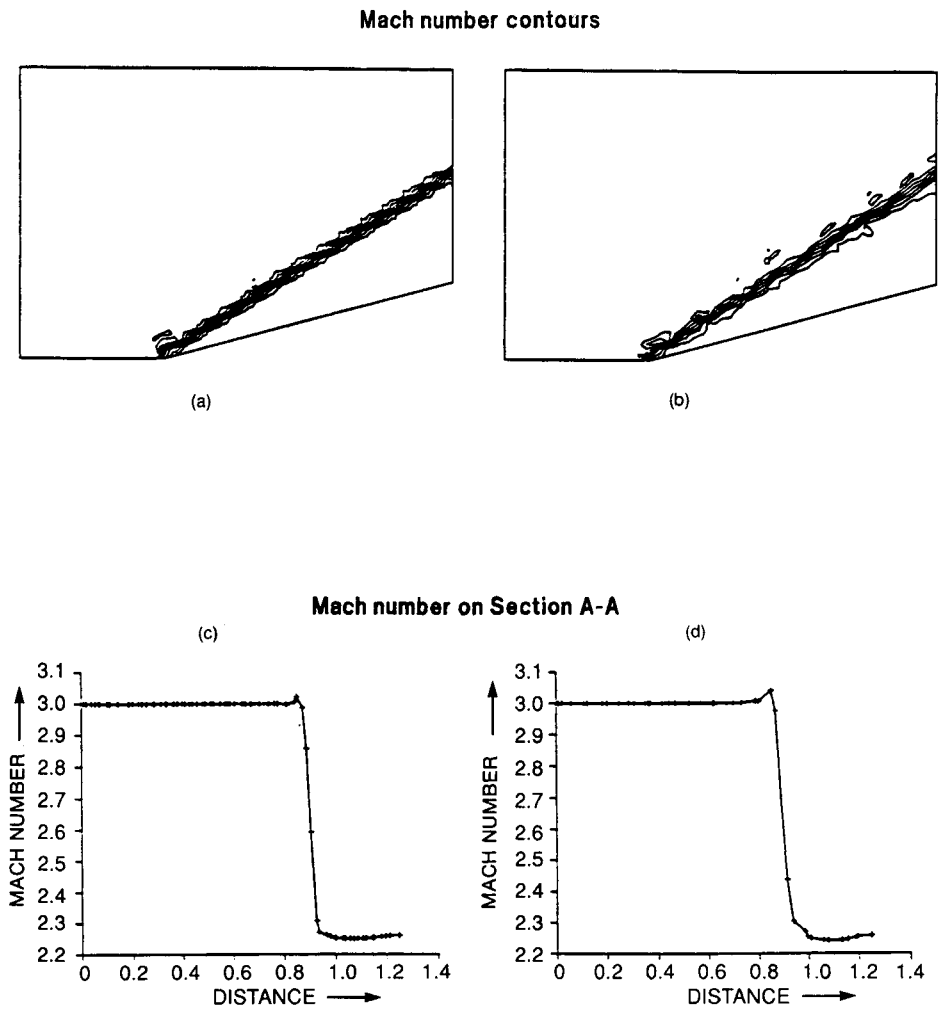

Figure 20. Problem of Figure 17 continued (Mach number): (a) contours with linear triangular elements; (b) contours with quadratic triangular elements; (c) distribution along the section with linear triangular elements; (d) distribution along the section with quadratic triangular elements

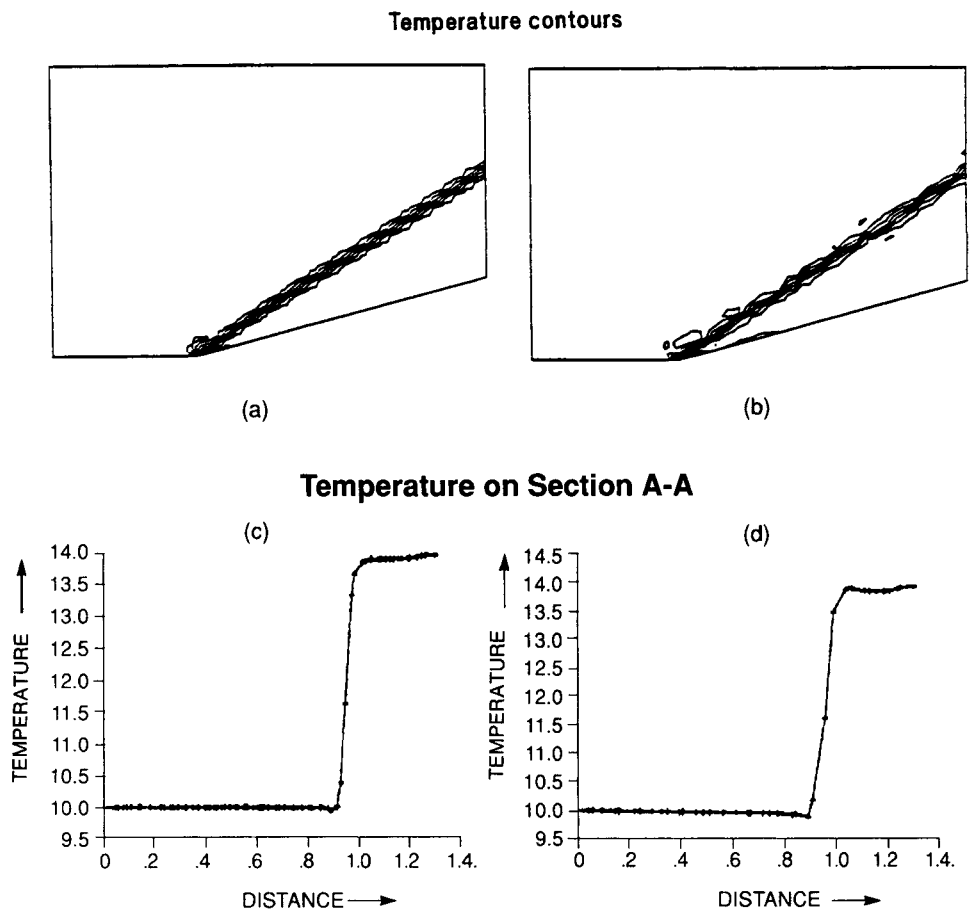

Figure 21. Problem of Figure 17 continued (temperature) (a) contour with linear triangular elements; (b) contours with quadratic triangular elements; (c) distribution along the section with linear triangular elements; (d) distribution along the section with quadratic triangular elements

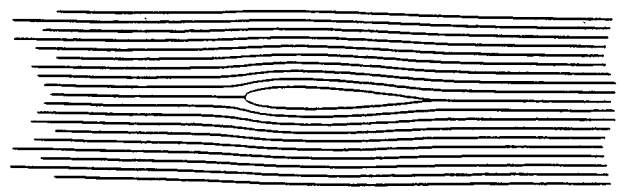

(a)

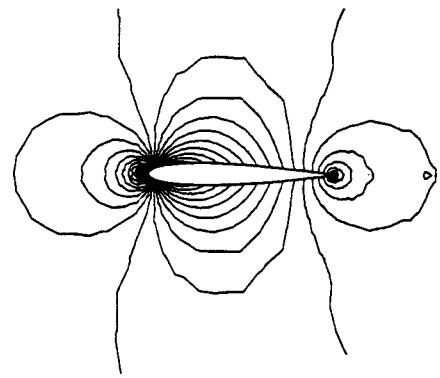

(b)

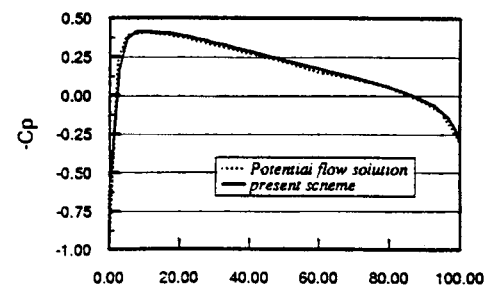

(c)

Figure 22. Inviscid incompressible flow past NACA0012 aerofoil with $\alpha = 0°$; (a) streamline pattern; (b) pressure contours; (c) comparison of coefficient of pressure with potential flow theory

contours, respectively. Figure 23(e) shows a comparison of horizontal velocity (u_1) along the mid-vertical plane of the cavity with that of Ghia *et al.*[7] It appears that the present scheme yields reasonably good results for the case considered.

The last two examples show that the fully explicit scheme can be applied to incompressible flow problems with success.

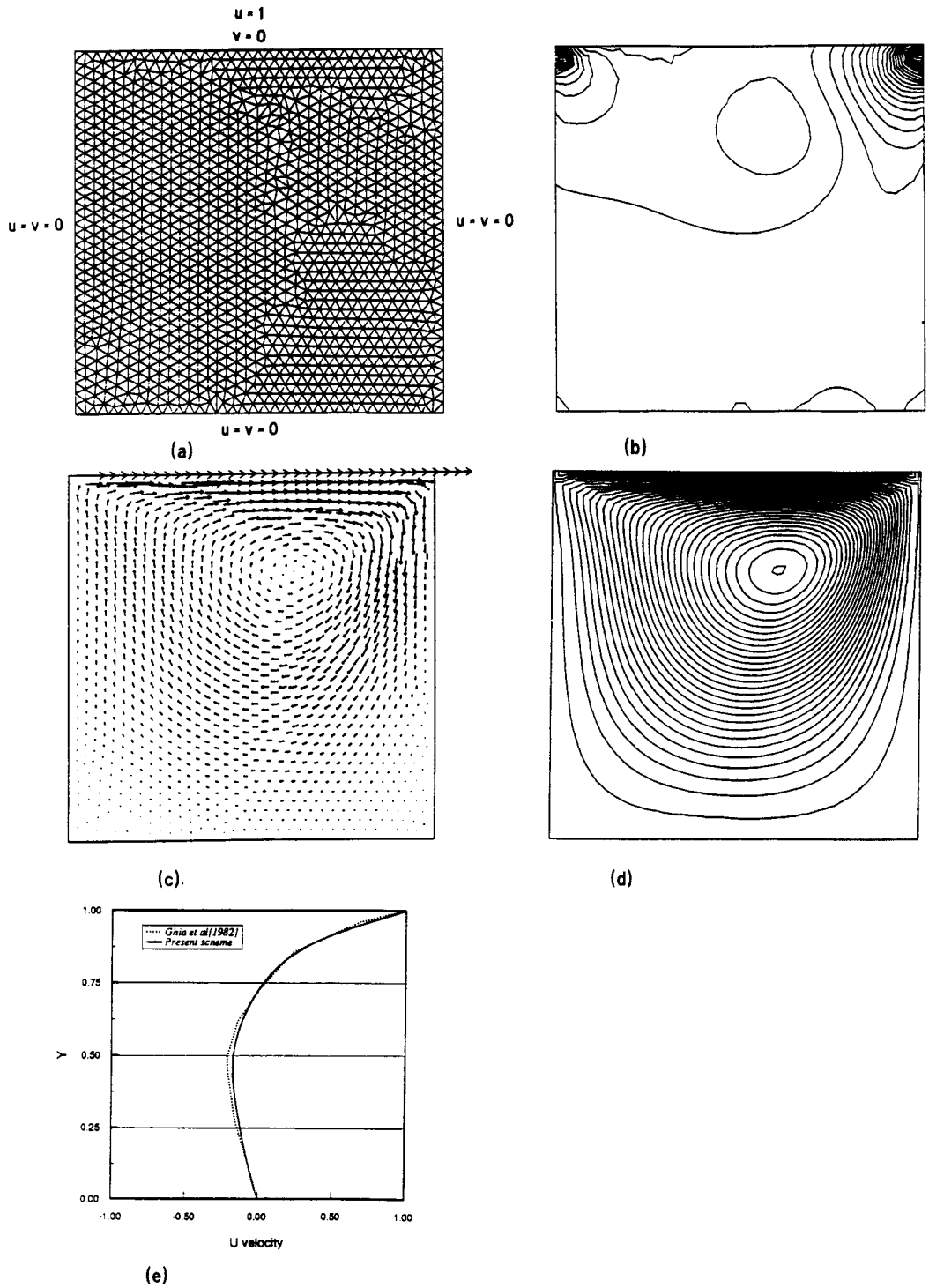

Figure 23. Lid-driven cavity problem ($Re = 100$): (a) mesh: no. of nodes = 1310, no. of elements = 2482; (b) pressure contours; (c) velocity vectors; (d) streamline pattern; (e) comparison of u_1 velocity along mid-vertical plane

6. CONCLUSIONS

The explicit form of the algorithm suggested in Part I of this paper has been tested on a variety of problems with considerable success. It appears that it is valid throughout the flow range and that it yields an accuracy which is at least equal to the other algorithms presently used without introducing artificial parameters. Only in the case of fully incompressible, transient, flow the explicit scheme is not applicable although, of course, here the semi-explicit form is optimally used. We shall address this semi-explicit formulation in Part III of the paper in detail.

Preliminary tests show that the use of higher-order interpolation is effective even in situations in which shocks develop. Certainly, for low Mach numbers such interpolation will be even more useful.

ACKNOWLEDGEMENT

The authors are grateful to NASA, who through their grant NAGW/2127 (AMES 90-144) supported this research.

REFERENCES

1. O. C. Zienkiewicz and R. Codina, 'A general algorithm for compressible and incompressible flow—Part I. The split, characteristic based scheme', *Int. j. numer. methods fluids*, **20,** 869–885 (1995).
2. J. Peraire, J. Peiro, L. Formaggia, K. Morgan and O. C. Zienkiewicz, 'Finite element Euler computations in three dimensions', *Int. j. numer. methods eng.*, **26,** 2135–2159 (1988).
3. O. C. Zienkiewicz and R. L. Taylor, *Finite Element Method*, Vol II, 4th edn, Mc-Graw Hill. New York, 1991.
4. T. H. Pulliam and J. T. Barton, 'Euler computations of AGARD Working Group 07 aerofoil test cases', *AIAA 23rd Aerospace Sciences Meeting*, 14–17 January 1985, Reno, Nevada.
5. O. C. Zienkiewicz and J. Wu 'Automatic directional refinement in adaptive analysis of compressible flows', *Int. j. numer. methods eng.*, **37**, 2189–2210 (1994).
6. O. Hassan, K. Morgan and J. Peraire, 'An implicit finite element method for high speed flows', 28th Aerospace Meeting, 1990, Reno, Nevada.
7. U. Ghia, K. N. Ghia and C. T. Shin, 'High-Re solution for incompressible flow using the Navier–Stokes equations and a multigrid method', *J. Comp. Phys.*, **48**, 387–411 (1982).